Author/s:
Messalea, KA;Zavabeti, A;Mohiuddin, M;Syed, N;Jannat, A;Atkin, P;Ahmed, T;Walia, S;McConville, CF;Kalantar-Zadeh, K;Mahmood, N;Khoshmanesh, K;Daeneke, T

Title:
Two-Step Synthesis of Large-Area 2D Bi2S3 Nanosheets Featuring High In-Plane Anisotropy

Date:
2020-11-01

Citation:
Messalea, K. A., Zavabeti, A., Mohiuddin, M., Syed, N., Jannat, A., Atkin, P., Ahmed, T., Walia, S., McConville, C. F., Kalantar-Zadeh, K., Mahmood, N., Khoshmanesh, K. & Daeneke, T. (2020). Two-Step Synthesis of Large-Area 2D Bi2S3 Nanosheets Featuring High In-Plane Anisotropy. Advanced Materials Interfaces, 7 (22), https://doi.org/10.1002/admi.202001131.

Two Step Synthesis of Large Area 2D Bi_2S_3 Nanosheets Featuring High In-Plane Anisotropy

Kibret A. Messalea[1], Ali Zavabeti[1,3], Md Mohiuddin[1], Nitu Syed[1], Azmira Jannat[1], Paul Atkin[1], Taimur Ahmed[1], Sumeet Walia[1], Chris F. McConville[2], Kourosh Kalantar-Zadeh[4], Nasir Mahmood[1], Khashayar Khoshmanesh[1], Torben Daeneke[1]*

[1] School of Engineering, RMIT University, Melbourne, Victoria 3000, Australia

[2] School of Science, RMIT University, Melbourne, Victoria 3000, Australia

[3] College of Material Science and Technology, Nanjing University of Aeronautics and Astronautics, 29 Jiangjun Ave., Nanjing 211100, Jiangsu, China

[4] School of Chemical Engineering, University of New South Wales (UNSW), Kensington, New South Wales, Australia

Corresponding Author Email: torben.daeneke@rmit.edu.au

This is the author manuscript accepted for publication and has undergone full peer review but has not been through the copyediting, typesetting, pagination and proofreading process, which may lead to differences between this version and the Version of Record. Please cite this article as doi: 10.1002/admi.202001131.

Abstract:

Two-dimensional (2D) materials with high in-plane anisotropy are rapidly emerging as a tantalizing class of nanomaterials with promising applications in nano-electronics and optoelectronics since they provide an additional degree of freedom that can be exploited in device design. The large area synthesis of such materials remains however challenging, since the anisotropic crystal structure renders identifying a suitable growth substrate to be difficult, while the nanosheets are usually too fragile for the exfoliation and transfer of macroscopic sheets.

This work reports the scalable synthesis of highly crystalline, large-area 2D Bi_2S_3 nanosheets using a novel liquid metal-based synthesis approach. Ultrathin bismuth oxide sheets are exfoliated from molten bismuth followed by tube furnace sulfurization. The strategy effectively separates the formation of layered structures from the process of anisotropic crystallization, overcoming the shortcomings of established techniques. The synthesized nanosheets feature a highly anisotropic orthorhombic crystal structure with intraplane van der Waals gaps and a direct bandgap of ~2.3 eV. The nanosheets were found to be highly photoconductive with a photoresponsivity of 8 AW^{-1}. Bi_2S_3 channel-based Field effect transistors feature a maximum hole mobility of 28 $cm^2V^{-1}s^{-1}$, highlighting the excellent electronic properties of the isolated nanosheets.

1. Introduction

In-plane anisotropic 2D nanomaterials emerged after the successful synthesis of black phosphorous (BP). Since then, multiple studies of polarization dependent properties have been reported[1]. Now, two dimensional materials with high in-plane anisotropy are entering the focus of the wider 2D materials research community due to their promising applications in electronics and optoelectronics[2]. Layered materials with anisotropic intralayer crystal structures feature direction dependent electronic, optical and phonon structures that result in marked differences in heat and charge transport along the different crystal axes[3]. The anisotropy also leads to optical excitation becoming highly polarization dependent[2b, 4]. These effects offer additional parameters that can be tuned and exploited in order to create novel devices such as polarization sensitive photodetectors and linearly polarized pulse generators[1a]. Moreover, the observed direction dependent conductance of anisotropic 2D nanosheets can be used in direction-sensitive sensors[1a, 3b, 5]. Furthermore, floating gate based anisotropic memory devices that provide multi-level outputs can be created with 2D nanosheets that possess large anisotropic conductance ratios[6]. These encouraging findings have led to an increased interest in the development of further anisotropic 2D nanostructures.

Bismuth sulfide (Bi_2S_3) is an archetypal anisotropic layered material from the stibnite family.[7] Bi_2S_3 exhibits interesting physical properties such as strong spin-orbit coupling which in turn influences its optoelectronic properties.[8] It also has excellent thermoelectric properties due to the small effective carrier masses and low thermal conductivity[8-9]. Additionally, Bi_2S_3 features a thickness dependent direct bandgap that can be tuned between 1.3 eV (bulk) and ~2.0 eV, rendering 2D Bi_2S_3 an optimal material for optoelectronic applications in the visible spectrum[10].

The crystal structure of Bi_2S_3 features van der Waals (vdW) strings. These strings consist of atoms that are bound covalently in one direction[7, 11]. Van der Waals forces arise between individual strings, and as such the Bi_2S_3 crystal exhibits weak vdW bonds along the other two dimensions[7]. This crystal structure is highly anisotropic and thus results in directional electrical, optical and mechanical properties [1a, 3b, 7].

The presence of vdW gaps along two axes also renders synthesizing large scale 2D Bi_2S_3 nanosheets to be challenging. The crystal easily fractures along the vdW gaps, and thus nanosheet synthesis *via* bulk exfoliation often results in undesired fragmentation due to the brittle nature of the material[7]. For instance, liquid exfoliation of Bi_2S_3 bulk powders leads to the formation of 1D nano-structures due to exfoliation occurring along both van der Waals gaps within the crystal[7].

Bottom-up synthesis approaches such as chemical vapor deposition (CVD) and molecular beam epitaxy (MBE) are equally challenging since they require carefully matched substrates in order to induce 2D growth while suppressing growth in the third dimension[12]. The complex crystal structures of high anisotropy 2D materials render substrate selection to be difficult. CVD and MBE growth methods also face limitations since multisite nucleation often results in abundant grain boundaries and inhomogeneous thickness within the material, while the slow growth rate often leads to prohibitively high costs[13]. As such, scalable new synthesis methods for the growth of large-area highly anisotropic 2D nanosheets of materials such as Bi_2S_3 are required.

To overcome the challenges of synthesizing 2D Bi_2S_3 nanosheets, a novel two-step synthesis method is proposed. The first crucial step is the synthesis of large area Bi_2O_3 nanosheets, which do not feature in plane vdW gaps[14]. The Bi_2O_3 sheets are mechanically robust and can

tolerate required processing steps[14]. The second step is the sulfurization of the Bi_2O_3 nanosheets once they are in place, converting the oxide into Bi_2S_3 nanosheets.

Recently, wafer-scale 2D metal oxides have been synthesized using self-limiting surface oxidation phenomena occurring on low temperature melting liquid metals such as Ga, In, Sn, and Bi[15]. The grown ultra-thin metal oxide layers can be delaminated onto any desired substrate and surfaces with relative ease, and further processing allows conversion of the oxides into chalcogenides, halides and pnictogenides, providing a new pathway towards the scalable synthesis of a plethora of nanomaterials for diverse applications[15e, 15f, 16].

Here, we report the large area two-step syntheses of high quality orthorhombic single-crystalline Bi_2S_3 2D nanosheets via sulfurization of 2D Bi_2O_3 nanosheets. The Bi_2O_3 nanosheets are exfoliated from the surface of liquid bismuth (**Figure S1**). The oxygen concentration during the oxide synthesis step was found to affect the thickness of the synthesized Bi_2O_3 which in turn provides control over the 2D Bi_2S_3 thickness. Sulfurization was then achieved in a tubular furnace at temperatures below 450°C. The obtained 2D Bi_2S_3 nanosheets were found to retain their sheet morphology and as such separating the formation of two dimensional nanosheets from the crystallization in a highly anisotropic stibnite crystal structure proved to be a promising approach towards the efficient and scalable growth of large area crystalline Bi_2S_3.

2. Synthesis and Characterization of 2D Bi_2S_3

Bi_2S_3 nanosheets were obtained using a two-step synthesis method. Firstly, Bi_2O_3 nanosheets were exfoliated from the surface of molten bismuth (Figure S1), then the ultrathin Bi_2O_3 nanosheets were converted into stoichiometric Bi_2S_3 *via* a tube furnace sulfurization process (**Figure 1a**). The sulfurization process was performed at relatively low temperature, so that structural damage resulting from exposing few layer thick nanosheets to high temperatures was kept to a minimum. Figure 1b presents the optical images of Bi_2S_3 nanosheets synthesized on SiO_2/Si substrates. It is evident from the optical images that ultrathin layers of Bi_2S_3 nanosheets were grown with lateral dimensions in the range of millimeters. Figure 1c, 1d & 1e depict three-unit cell thick Bi_2S_3, highlighting the van der Waals string type crystal structure with significant in-plane anisotropy. The thickness of the nanosheet was measured using atomic force microscopy (AFM), revealing that the nanosheets exhibit edge folding and tend to be flat within the field of view of the AFM. Edge folding is frequently observed in liquid metal exfoliated nanosheets[17]. The thickness of the material was found to be governed by the lattice parameters of the unit cell. A typical AFM image of bilayer Bi_2S_3 is shown in Figure 1f & 1g, with additional AFM images being presented in supplementary **Figure S2**.

Transmission electron microscopy (TEM) was used to reveal the atomic structure and orientation of the synthesized Bi_2S_3. **Figure 2a** shows the morphology of a Bi_2S_3 nanosheet that was synthesized on a high temperature chemically resistant silicon nitride TEM grid. The nanosheets obtained were found to be laterally large and ultrathin. Cracks visible within the TEM image likely arise due to the holes in the silicon nitride membrane. High resolution TEM (HRTEM) was carried out to assess the crystal structure of the nanosheet (Figure 2b). The HRTEM and selected area electron diffraction (SAED) patters in Figure 2c and Figure 2d confirm that the few nanometer thick nanosheets show excellent phase purity, since only

the (210) facets are visible with a typical crystal spacing of 3.2 Å. The crystal structure was also confirmed using scanning tunneling microscopy (STM) of the 2D nanosheets synthesized on conductive silicon wafers, highlighting that the preferred growth orientation appears to be substrate independent (**Figure S3**). Elemental mapping using energy-dispersive X-ray spectroscopy (EDX) was carried out to obtain the elemental distribution within the material (Figure 2e-g). Figure 2f and Figure 2g show EDX maps of S and Bi, respectively, highlighting that the isolated 2D nanosheets are homogeneously sulfurized.

X-ray photoelectron spectroscopy (XPS) was used to characterize the chemical stoichiometry of the synthesized nanosheets (**Figure 3a**). The Bi 4f spectrum shows dominant peaks at 158.4 and 163.7 eV related to Bi^{3+} $4f_{7/2}$ and Bi^{3+} $4f_{5/2}$ respectively[18]. The S 2s region (Figure 3b) features a peak at 225.1 eV which corresponds to sulfur chemically bound to bismuth, while the smaller peak at 228 eV is characteristic of the presence of elemental sulfur which likely arises due to small amounts of residual sulfur being deposited during the sulfurization process[19]. Within the O 1s region, a single peak at 533 eV is associated with the substrate Si-O-Si bonds[20]. The characteristic Bi-O peak that is typically observed at ~530 eV is absent, confirming that total replacement of oxygen with sulfur was achieved (Figure 3c, **Figure S4**)[14]. Furthermore, analysis of the XPS peak intensities revealed a bismuth to sulfur ratio of 0.67, which is consistent with stoichiometric Bi_2S_3[18a]. Analysis of the XPS valence band region reveals that the Fermi level is situated 0.9 eV above the valance band edge (Figure 3d). Tauc analysis of the UV-vis spectrum (Figure 3e, **Figure S5**) reveals that the 2D nanosheets have a direct optical bandgap of 2.3 eV. The combination of XPS valence band analysis and UV-vis data indicates that the ultrathin Bi_2S_3 is slightly p-type. The presence of a sparse layer of elemental sulfur deposited onto the Bi_2S_3 nanosheets during synthesis was found to affect the doping level of the nanosheets. Sheets with minimal elemental surface

sulfur exhibited nearly intrinsic behavior, while other nanosheets with more abundant surface sulfur exhibited XPS valence band spectra that are indicative of strong p-type doping (**Figure S7**).

The electronic bandgap was confirmed using scanning tunneling spectroscopy (STS) by plotting $\frac{dI}{dV}(V)$ as a function of the applied bias voltage (Figure S3). The result confirms that the bandgap is ~2.3 eV and that the nanosheets are p-type semiconductors. Bandgap analysis of thicker Bi_2S_3 nanosheets was also conducted (**Figure S6**). As the thickness increased from double layer (~2.5 nm) to few layers (~5 nm and ~8 nm) the band gap narrowed by ~50 meV and ~100 meV respectively, due to differing degrees of quantum confinement[5d]. A further increase in thickness to ~15 nm shifted the direct band gap to ~2.05 eV, while a thickness of ~100 nm resulted in a bandgap of 1.85 eV.

Figure 4f shows the Raman spectrum of the 2D nanosheets. The A_g Raman modes located at 100 and 237 cm^{-1} and the B_{1g} modes at 187 and 264 cm^{-1} correspond well with the theoretically predicted active Raman modes of 2D Bi_2S_3[21]. The A_g and B_{1g} modes are associated with transverse (TO) and longitudinal (LO) optical phonons. Overall the Raman spectrum is consistent with highly crystalline ultrathin 2D Bi_2S_3 nanosheets[21b].

Photoluminescence (PL) spectroscopy was performed at room temperature with a 532 nm excitation source to study the optical properties of the 2D nanosheets further and to detect impurity and defect states that may be associated with the sulfurization process. The PL spectrum (**Figure 4a**) features a broad peak at 624 nm which corresponds well to the expected emission from the observed optical bandgap. The observed broad PL spectrum is a result of the involvement of multiple transitions and the presence of surface trap-states, which

cannot be sufficiently resolved at room temperature[22]. PL spectra for thicker samples are shown in **Figure S8**, revealing a PL peak shift and thickness dependent emission profile.

PL mapping conducted on an edge-near area (Figure 4b and c) revealed that the nanosheets feature relatively homogeneous luminescent properties with enhanced emission near the edges of the nanosheet which is commonly observed in 2D materials[23]. The PL map indicates that the 2D nanosheets feature high homogeneity and possess consistent electronic properties across large areas.

The in-plane anisotropy of the Bi_2S_3 nanosheets was investigated using angle-resolved Raman spectroscopy. Before using polarized Raman spectroscopy, unpolarized Raman spectra were recorded to identify all active modes (Figure 4d). The Raman modes of the 2D nanosheets shifted towards higher wave numbers when compared with bulk Bi_2S_3 samples. Such a shift can be associated with decreased long-range Coulombic interaction in few layer nanosheets[5c, 24]. The Raman setup for angle dependent polarized measurements is illustrated in **Figure S9**. The excitation laser and analyzer are polarized perpendicularly and the nanosheets can be aligned within the stage's X-Y plane. The measurement was performed by rotating the polarizer angles while keeping the sample in a fixed position (**Figure S10**). As illustrated previously, the visible Raman modes of 2.5 nm thick Bi_2S_3 are B_{1g} and A_{1g}. Therefore, one representative mode (A_{1g} at 240 cm^{-1}) was selected in order to study the in-plane anisotropy of the Bi_2S_3 nanosheet. The polarization dependent intensity plot (Figure 4e) clearly shows the expected two lobe shape that arises from the 1D arrangement within the stibnite structure[4, 5b, 5c]. These measurements also confirmed that the Bi_2S_3 nanosheets grow along the (210) direction which is consistent with HRTEM as well as STM results. As such, the polarized Raman spectroscopy method may be utilized to assist future device manufacturing as a non-destructive tool for the identification of the growth direction. This

may be required when electrode alignment with the crystal structure is critical, particularly in light of the high degree of anisotropy [25].

3. 2D Bi_2S_3 based Electronic and Optoelectronic Devices

The observed direct bandgap of ~ 2.3 eV[26] and high crystallinity renders the synthesized Bi_2S_3 nanosheets to be excellent candidates for electronic devices and high-sensitivity visible light optoelectronics[27]. To showcase their viability for practical applications, Bi_2S_3 nanosheet based field-effect transistors (FETs) were fabricated using standard lithography, thermal evaporation and lift off processes in a back gate configuration. Cr/Au (5/50 nm) contacts were deposited, were Cr functions as an adhesion layer between Au and Bi_2S_3. **Figure 5a** shows the electrical characteristics of a typical Bi_2S_3 nanosheet FET device with a channel width of 20 µm and channel length of 2 µm. The ON/OFF ratio of the device was found to be ~ 10^3 with clear p-type behavior (Figure 5b).

The FET devices featured a comparatively high ON state current at V_{ds} = 200 mV of 0.3 µA (Figure 5a). The hole mobility was calculated using the transconductance as a function of the back-gate voltage (V_{bg}) in the range of -40 < V_{bg} < 40 V using equation (1),

$$\mu = \frac{L}{W}\frac{1}{C_{ox}}\frac{dI_{ds}}{dV_{bg}}\frac{1}{V_{ds}} \qquad (1)$$

where L is the length of the channel, W is the channel width, C_{ox} is the capacitance of 300 nm SiO_2, dI_{ds}/dV_{bg} is the measured transconductance of the channel, and V_{bg} is the back-gate voltage. The dielectric capacitance can be expressed using equation (2),

$$C_{ox} = \frac{\varepsilon_o \varepsilon_r}{d_{ox}} \qquad (2)$$

where the oxide thickness d_{ox} is 300 nm, the relative permittivity ε_r of SiO_2 is 3.9, and the free space permittivity ε_o is 8.87×10^{-12} F.m^{-1}

The mean mobility at room temperature was found to be 12.4 $cm^2V^{-1}s^{-1}$ with a standard deviation of 9.1 $cm^2V^{-1}s^{-1}$ and a maximum mobility as high as ~28 $cm^2V^{-1}s^{-1}$ for the best performing device. The high standard deviation of the mobility from the mean value likely arises from the anisotropy of the 2D Bi_2S_3 nanosheets, where carrier transport along the 1D van der Waals strings is expected to be significantly favored compared to transport across the vdW gap. Compared to other layered p-type 2D semiconductors with a similar thickness such as GaS, Ga_2S_3, MoS_2, ReS_2 and In_2S_3, the observed mobility of the 2D Bi_2S_3 nanosheets was found to be at par[5a, 28]. This highlights that the developed synthesis strategy is capable of producing 2D nanosheets with excellent electronic properties, equivalent to what can be achieved *via* CVD and exfoliation strategies. Furthermore, the Bi_2S_3 nanosheets were found to show excellent stability in air, with Raman spectra taken on as synthesized nanosheets and after three months of storage being indistinguishable (**Figure S11**).

A two terminal device was designed on a SiO_2/Si substrate to measure the photoresponse of 2D Bi_2S_3 nanosheets (**Figure S12**). The photoresponse of the device under different light intensities as well as the dark current for a bias voltage of -2 V < V_{ds}< 2 V is shown in Figure 5c. The transient response of the device is shown in Figure 5d, revealing a rise time τ_r = 80 ms where τ_r is the time required for the photodetector to increase its output from 10 % to 90 % of the final output level **(Figure S13). Figure S14** shows the current density with respect to the applied voltage. The operational bandwidth (BW) was estimated using the approximation BW = $0.35/\tau_r$, resulting in an operational bandwidth of 4.38 Hz. While the low BW will limit the Bi_2S_3 nanosheets suitability for high speed optical applications in the current device configuration. Further optimization of the device dimensions, dielectric

environment and electrode design are expected to significantly improve the response time and bandwidth. The responsivity (R_λ), defined as the photocurrent generated per unit power of the incident light for the effective area of the photodetector, can be calculated using $R_\lambda = \frac{\Delta I}{PA}$ where ΔI is difference between photocurrent under illumination and the dark current, P is the intensity of the incident light and A is the effective area [29]. The 2D Bi_2S_3 based photodetector responsivity was calculated with an applied potential V_{DS} of 2V, light intensity P of 2 mW/cm^2, measured effective area A of 100 μm^2 as shown in Figure S12, and measured ΔI = 16 nA. This calculated responsivity of 8 AW^{-1} exceeds that of many existing and widely used silicon based photodetectors[30]. This finding suggests that the Bi_2S_3 nanosheet based photodetector may enable applications in sensing electronics.

A recent report of bismuth sulfide-based photodetectors that were fabricated using few layer nanosheets with lateral sizes below 120 nm reported a responsivity of 210 μAW^{-1}. [31] This is roughly ~ 38,000 times lower when compared to this work. This comparison clearly highlights the importance of utilizing large single sheets rather than composite films that are composed of many nano discs and rods. Additionally, the rise time observed in this work was ~ 1.25 times faster when compared with the preceding report of a 2D Bi_2S_3 photodetector

4. Conclusions

In summary, high-quality 2D Bi_2S_3 nanosheets have been successfully synthesized using a two step-synthesis method. The as synthesized nanosheets feature lateral sizes reaching several millimeters, while typically being 2.5 nm thick. The isolated nanosheets featured high phase purity and excellent crystallinity. These findings highlight that the developed liquid metal-based synthesis technique is well suited for the synthesis of large-area 2D nanosheets of stibnite-type materials. This achievement is particularly noteworthy since stibnites as well

as the closely related tetradymites, feature a 1D van der Waals string-type structure that usually results in the formation of nanobelts and nanowires rather than planar nanosheets.

The high crystallinity and large lateral size allowed the fabrication of back-gated FETs to study the electronic properties of the nanosheets. The 2D Bi_2S_3 nanosheets were found to be p-type semiconductors with a maximum hole mobility of 28 $cm^2V^{-1}s^{-1}$ at room temperature. This is comparable with the carrier mobility of CVD grown 2D materials such as MoS_2[32]. The 2D Bi_2S_3 nanosheets exhibited a photoresponsivity of 8 AW^{-1}. As such these 2D Bi_2S_3 nanosheets may well find application in a range of future electronic devices that take advantage of the high anisotropy of stibnites. Furthermore, this method may also be well suited to for the large-scale synthesis of tetradymites such as Bi_2Se_3 and Bi_2Te_3 which are both well-known topological insulators.

5. Experimental section

Materials: Bismuth (Bi, 99.98%) and sulfur (S, 99.99%) were purchased from Roto Metals and Alfa Aesar respectively. All chemicals were used as received.

Synthesis of single crystal Bi_2S_3 nanosheets : The Bi_2S_3 nanosheets were grown on SiO_2/Si, glass slides, quartz slides and TEM grids using a twostep synthesis method. First, the Bi_2O_3 nanosheets were printed on suitable substrates using the liquid metal synthesis method described (Figure S1). The liquid metal synthesis method relies on delaminating the surface oxide that forms on liquid metal due to Cabrera-Mott oxidation in a controlled oxygen environment (~ 100 ppm O_2). Bismuth metal was melted on a glass slide inside a flow-through N_2 glove-box. The molten droplet was then squeezed using another glass slide to remove existing oxides following a previously described preconditioning technique[15b].

Touch printing with suitable substrates was then used to delaminate the Bi_2O_3 nanosheets. The Bi_2O_3 2D nanosheets were then converted to Bi_2S_3 nanosheets using a tube furnace. The closed system was first purged with N_2 before ramping up to the desired temperature for the growth of Bi_2S_3 (450 °C). Elemental sulfur was kept in a ceramic boat at the N_2 inlet side of the furnace at a position where the temperature was 200 °C. The 2D Bi_2O_3 samples were kept in the center of tube furnace where the temperature reached 450 °C. A ramping and deramping rate of 9 °C/min was chosen, while the dwell time at 450 °C was 15 minutes.

Characterization: An optical microscope (DP 27, OLYMPUS) was used to take images of the synthesized 2D nanosheets on SiO_2 substrates. The thickness of the nanosheets was characterized using an atomic force microscope (Bruker Dimension Icon AFM). TEM characterization was performed using JEOL 1010 and JEM-2100F TEM microscopes operating at 100kV and 200kV, respectively. Samples were synthesized on chemically and temperature resistant Si_3N_4 TEM girds (Ted Pella, 21587) by directly printing the Bi_2O_3 nanosheet on the TEM membranes followed by subsequent tube sulfurization. Raman and PL spectroscopy characterization were carried out using Horiba Scientific LabRAM HR evolution with a 532 nm laser excitation source. For PL measurements, a 150 grating/500nm was used. Optical absorption spectroscopy of samples was carried out on samples deposited on quartz slides. UV-visible-NIR spectra were collected with a CRAIC Microspectrophometer. All measurements were performed under ambient conditions. XPS analysis was conducted on samples printed on SiO_2/Si substrates. A Thermo Scientific K-alpha XPS spectrometer equipped with a monochromatic Al Kα source (h□ = ~ 1486.6 eV), and a concentric hemispherical analyzer (CHA) were used to determine the chemical composition of the 2D nanosheets. The analyzer was operated with a pass energy of 100 eV to record the core-level spectra and 50 eV to record the valance band spectra. A low-energy

electron flood gun was utilized to minimize any surface charging effects. Scanning tunneling microscopy (STM) was performed using an Omicron model VT. STM (Omicron Nanotechnology GmbH) based spectroscopy and imaging was acquired at room temperature using Matrix V4.3.7 software. STM imaging was conducted in constant current mode (0.5 nA) with a gap voltage of 1.4 V. The STM images were consequently filtered using Gwyddion software.

Device fabrication and characterization: The contact electrodes on top of the Bi_2S_3 nanosheets were realized with a mask-less photolithography process using a Mask-less Aligner MLA 150 (Heidelberg Instruments) and photoresist AZ 1512HS. Cr/Au (5/50 nm) electrodes were deposited using electron beam evaporation. Lift off was achieved by immersing the samples in acetone for 20 minutes, followed by an isopropyl alcohol cleaning step, exposing the patterned electrodes. Finally, FET characterization was conducted using a probe-station combined with a Keysight B2902A source-meter and the Keysight Quick IV measurement software.

Supporting Information

Supporting information is available from the Wiley Online Library or from the author.

Author Contributions

The manuscript was written through contributions of all authors. All authors have given approval to the final version of the manuscript.

Acknowledgments

We are grateful for access to the facilities and scientific and technical assistance of the RMIT Microscopy and Microanalysis Facility (RMMF) and the RMIT Micro Nano Research Facility (MNRF). The authors would also like to thank the Australian Research Council, Centre of Excellence for Future Low-Energy Electronics Technologies (FLEET - CE170100039) for financial support T.D. acknowledges funds received for the ARC DECRA Project DE190100100. K.A.M., K.K. and K.K.z acknowledge the Australian Research Council for financial support under Discovery Project DP170102138.

Conflict of Interest

No conflict of interest is declared.

Keywords

Two-dimensional 2D, nanosheets, bismuth sulfide Bi_2S_3, anisotropic, liquid metal, p-type semiconductor

Reference

[1] a) H. Lin, Q. Zhu, D. Shu, D. Lin, J. Xu, X. Huang, W. Shi, X. Xi, J. Wang, L. Gao, *Nat. Mater.* **2019**, 18, 602; b) T. Ahmed, S. Kuriakose, E. L. H. Mayes, R. Ramanathan, V. Bansal, M. Bhaskaran, S. Sriram, S. Walia, *Small* **2019**, 15, 1900966.

[2] a) S. Zhao, B. Dong, H. Wang, H. Wang, Y. Zhang, Z. V. Han, H. Zhang, *Nanoscale Adv.* **2020**, 2, 109; b) C. Wang, G. Zhang, S. Huang, Y. Xie, H. Yan, *Adv Opt Mater* **2020**, 8, 1900996; c) Y. Song, Z. Liang, X. Jiang, Y. Chen, Z. Li, L. Lu, Y. Ge, K. Wang, J. Zheng, S. Lu, J. Ji, H. Zhang, *2D Mater.* **2017**, 4, 045010.

[3] a) Y. An, Y. Hou, K. Wang, S. Gong, C. Ma, C. Zhao, T. Wang, Z. Jiao, H. Wang, R. Wu, *Adv. Func. Mater.* **2020**, n/a, 2002939; b) B. Majérus, E. Dremetsika, M. Lobet, L. Henrard, P. Kockaert, *Phys. Rev. B* **2018**, 98, 125419; c) Z. Li, H. Qiao, Z. Guo, X. Ren, Z. Huang, X. Qi, S. C. Dhanabalan, J. S. Ponraj, D. Zhang, J. Li, J. Zhao, J. Zhong, H. Zhang, *Adv. Func. Mater.* **2018**, 28, 1705237.

[4] Z. Zhou, Y. Cui, P.-H. Tan, X. Liu, Z. Wei, *J. Semicond.* **2019**, 40, 061001.

[5] a) M. Rahman, K. Davey, S.-Z. Qiao, *Adv. Func. Mater.* **2017**, 27, 1606129; b) S. Niu, G. Joe, H. Zhao, Y. Zhou, T. Orvis, H. Huyan, J. Salman, K. Mahalingam, B. Urwin, J. Wu, Y. Liu, T. E. Tiwald, S. B. Cronin, B. M. Howe, M. Mecklenburg, R. Haiges, D. J. Singh, H. Wang, M. A. Kats, J. Ravichandran, *Nat. Photonics* **2018**, 12, 392; c) H. Song, T. Li, J. Zhang, Y. Zhou, J. Luo, C. Chen, B. Yang, C. Ge, Y. Wu, J. Tang, *Adv. Mater.* **2017**, 29, 1700441; d) M. Zhao, J. Su, Y. Zhao, P. Luo, F. Wang, W. Han, Y. Li, X. Zu, L. Qiao, T. Zhai, *Adv. Func. Mater.* **2020**, 30, 1909849.

[6] H. Wang, M.-L. Chen, M. Zhu, Y. Wang, B. Dong, X. Sun, X. Zhang, S. Cao, X. Li, J. Huang, L. Zhang, W. Liu, D. Sun, Y. Ye, K. Song, J. Wang, Y. Han, T. Yang, H.

Guo, C. Qin, L. Xiao, J. Zhang, J. Chen, Z. Han, Z. Zhang, *Nat. Commun.* **2019**, 10, 2302.

[7] N. Dhar, N. Syed, M. Mohiuddin, A. Jannat, A. Zavabeti, B. Y. Zhang, R. S. Datta, P. Atkin, N. Mahmood, D. Esrafilzadeh, T. Daeneke, K. Kalantar-Zadeh, *ACS Appl. Mater. Interfaces* **2018**, 10, 42603.

[8] R. Chmielowski, D. Péré, C. Bera, I. Opahle, W. Xie, S. Jacob, F. Capet, P. Roussel, A. Weidenkaff, G. K. H. Madsen, G. Dennler, *J Appl Phys* **2015**, 117, 125103.

[9] J. P. Heremans, R. J. Cava, N. Samarth, *Nat. Rev. Mater.* **2017**, 2, 17049.

[10] L. Cademartiri, R. Malakooti, P. G. O'Brien, A. Migliori, S. Petrov, N. P. Kherani, G. A. Ozin, *Angew. Chem. Int. Ed.* **2008**, 47, 3814.

[11] R. M. Clark, J. C. Kotsakidis, B. Weber, K. J. Berean, B. J. Carey, M. R. Field, H. Khan, J. Z. Ou, T. Ahmed, C. J. Harrison, I. S. Cole, K. Latham, K. Kalantar-zadeh, T. Daeneke, *Chem. Mater.* **2016**, 28, 8942.

[12] a) C. Tan, H. Zhang, *Nat. Commun.* **2015**, 6, 7873; b) M. Chhowalla, H. S. Shin, G. Eda, L.-J. Li, K. P. Loh, H. Zhang, *Nat. Chem.* **2013**, 5, 263.

[13] a) Y. Ma, B. Li, S. Yang, *Mater. Chem. Front.* **2018**, 2, 456; b) H. Zhang, *ACS Nano* **2015**, 9, 9451.

[14] K. A. Messalea, B. J. Carey, A. Jannat, N. Syed, M. Mohiuddin, B. Y. Zhang, A. Zavabeti, T. Ahmed, N. Mahmood, E. Della Gaspera, K. Khoshmanesh, K. Kalantar-Zadeh, T. Daeneke, *Nanoscale* **2018**, 10, 15615.

[15] a) A. Zavabeti, J. Z. Ou, B. J. Carey, N. Syed, R. Orrell-Trigg, E. L. H. Mayes, C. Xu, O. Kavehei, A. P. O'Mullane, R. B. Kaner, K. Kalantar-zadeh, T. Daeneke, *Science* **2017**, 358, 332; b) T. Daeneke, P. Atkin, R. Orrell-Trigg, A. Zavabeti, T. Ahmed, S. Walia, M. Liu, Y. Tachibana, M. Javaid, A. D. Greentree, S. P. Russo, R. B. Kaner, K. Kalantar-Zadeh, *ACS Nano* **2017**, 11, 10974; c) B. J. Carey, J. Z. Ou, R. M. Clark,

K. J. Berean, A. Zavabeti, A. S. R. Chesman, S. P. Russo, D. W. M. Lau, Z.-Q. Xu, Q. Bao, O. Kavehei, B. C. Gibson, M. D. Dickey, R. B. Kaner, T. Daeneke, K. Kalantar-Zadeh, *Nat. Commun.* **2017**, 8, 14482; d) A. Jannat, Q. Yao, A. Zavabeti, N. Syed, B. Y. Zhang, T. Ahmed, S. Kuriakose, M. Mohiuddin, N. Pillai, F. Haque, G. Ren, D. M. Zhu, N. Cheng, Y. Du, S. A. Tawfik, M. J. S. Spencer, B. J. Murdoch, L. Wang, C. F. McConville, S. Walia, T. Daeneke, L. Zhu, J. Z. Ou, *Mater. Horiz.* **2020**, 7, 827; e) N. Syed, A. Zavabeti, K. A. Messalea, E. Della Gaspera, A. Elbourne, A. Jannat, M. Mohiuddin, B. Y. Zhang, G. Zheng, L. Wang, S. P. Russo, E. Dorna, C. F. McConville, K. Kalantar-Zadeh, T. Daeneke, *J. Am. Chem. Soc.* **2019**, 141, 104; f) N. Syed, A. Zavabeti, J. Z. Ou, M. Mohiuddin, N. Pillai, B. J. Carey, B. Y. Zhang, R. S. Datta, A. Jannat, F. Haque, K. A. Messalea, C. Xu, S. P. Russo, C. F. McConville, T. Daeneke, K. Kalantar-Zadeh, *Nat. Commun.* **2018**, 9, 3618; g) R. S. Datta, N. Syed, A. Zavabeti, A. Jannat, M. Mohiuddin, M. Rokunuzzaman, B. Yue Zhang, M. A. Rahman, P. Atkin, K. A. Messalea, M. B. Ghasemian, E. D. Gaspera, S. Bhattacharyya, M. S. Fuhrer, S. P. Russo, C. F. McConville, D. Esrafilzadeh, K. Kalantar-Zadeh, T. Daeneke, *Nat. Electron.* **2020**, 3, 51.

[16] A. Zavabeti, A. Jannat, L. Zhong, A. A. Haidry, Z. Yao, J. Z. Ou, *Nano-Micro Lett.* **2020**, 12.

[17] P. Atkin, R. Orrell-Trigg, A. Zavabeti, N. Mahmood, M. R. Field, T. Daeneke, I. S. Cole, K. Kalantar-zadeh, *Chem. Commun.* **2018**, 54, 2102.

[18] a) M. Bernechea, Y. Cao, G. Konstantatos, *J. Mater. Chem. A* **2015**, 3, 20642; b) A. Helal, F. A. Harraz, A. A. Ismail, T. M. Sami, I. A. Ibrahim, *Appl. Catal. B: Environ.* **2017**, 213, 18.

[19] a) H. Song, X. Zhan, D. Li, Y. Zhou, B. Yang, K. Zeng, J. Zhong, X. Miao, J. Tang, *Sol. Energy Mater. Sol. Cells* **2016**, 146, 1; b) R. Malakooti, L. Cademartiri, Y. Akçakir, S. Petrov, A. Migliori, G. A. Ozin, *Adv. Mater.* **2006**, 18, 2189.

[20] J. Pourasad, N. Ehsani, S. A. Khalifesoltani, *J. Eur. Ceram. Soc.* **2016**, 36, 3947.

[21] a) I. Zumeta-Dubé, J.-L. Ortiz-Quiñonez, D. Díaz, C. Trallero-Giner, V.-F. Ruiz-Ruiz, *J. Phys. Chem. C* **2014**, 118, 30244; b) Y. Zhao, K. T. E. Chua, C. K. Gan, J. Zhang, B. Peng, Z. Peng, Q. Xiong, *Phys. Rev. B* **2011**, 84, 205330.

[22] Y. A. Haleem, Q. Di, B. Bai, M. Xu, W. Chen, J. Liu, J. Liu, H. Rong, J. Zhang, *J. Mater. Chem. C* **2019**, 7, 13849.

[23] Z. Jiang, G. B. Bhandari, S. M. Prematilaka, S. Khan, D. M. Dimick, C. Stombaugh, A. Mandell, Y. He, H. Peter Lu, L. Sun, *Phys. Chem. Chem. Phys.* **2015**, 17, 23303.

[24] H. R. Gutiérrez, N. Perea-López, A. L. Elías, A. Berkdemir, B. Wang, R. Lv, F. López-Urías, V. H. Crespi, H. Terrones, M. Terrones, *Nano Lett.* **2013**, 13, 3447.

[25] S. Wood, G.-P. Rigas, A. Zoladek-Lemanczyk, J. C. Blakesley, S. Georgakopoulos, M. Mas-Torrent, M. Shkunov, F. A. Castro, *Sci. Rep.* **2016**, 6, 33057.

[26] M. Aresti, M. Saba, R. Piras, D. Marongiu, G. Mula, F. Quochi, A. Mura, C. Cannas, M. Mureddu, A. Ardu, G. Ennas, V. Calzia, A. Mattoni, A. Musinu, G. Bongiovanni, *Adv. Func. Mater.* **2014**, 24, 3341.

[27] G. Konstantatos, L. Levina, J. Tang, E. H. Sargent, *Nano Lett.* **2008**, 8, 4002.

[28] J. Xu, L. Chen, Y.-W. Dai, Q. Cao, Q.-Q. Sun, S.-J. Ding, H. Zhu, D. W. Zhang, *Sci. Adv.* **2017**, 3, e1602246.

[29] a) P. Hu, L. Wang, M. Yoon, J. Zhang, W. Feng, X. Wang, Z. Wen, J. C. Idrobo, Y. Miyamoto, D. B. Geohegan, K. Xiao, *Nano Lett.* **2013**, 13, 1649; b) J. Yin, Z. Tan, H. Hong, J. Wu, H. Yuan, Y. Liu, C. Chen, C. Tan, F. Yao, T. Li, Y. Chen, Z. Liu, K. Liu, H. Peng, *Nat. Commun.* **2018**, 9, 3311.

[30] a) G. Konstantatos, *Nat. Commun.* **2018**, 9, 5266; b) M. Long, P. Wang, H. Fang, W. Hu, *Adv. Func. Mater.* **2019**, 29, 1803807.

[31] W. Huang, C. Xing, Y. Wang, Z. Li, L. Wu, D. Ma, X. Dai, Y. Xiang, J. Li, D. Fan, H. Zhang, *Nanoscale* **2018**, 10, 2404.

[32] M. D. Siao, W. C. Shen, R. S. Chen, Z. W. Chang, M. C. Shih, Y. P. Chiu, C. M. Cheng, *Nat. Commun.* **2018**, 9, 1442.

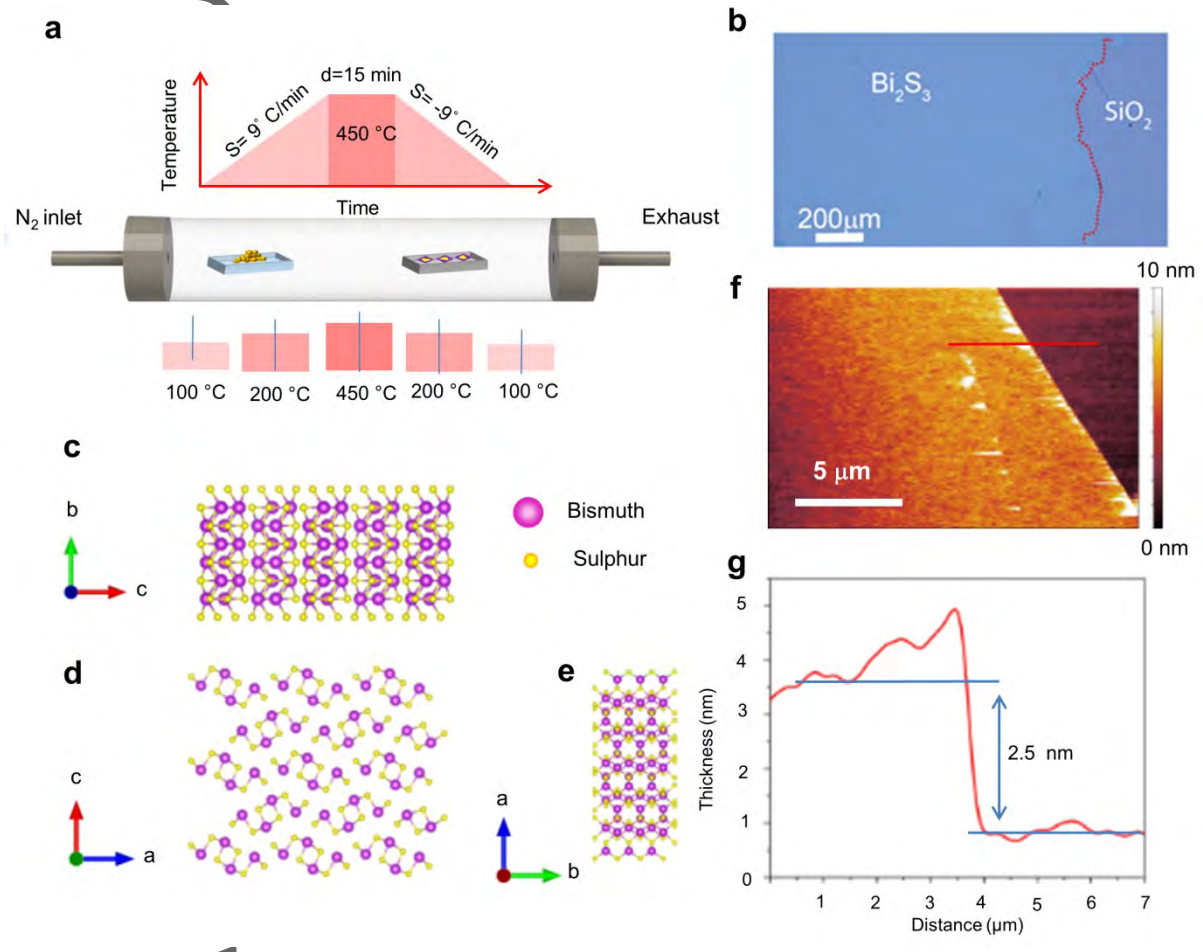

Figure 1. (a) Schematic of the tube furnace sulfurization process used to convert Bi_2O_3 nanosheets to Bi_2S_3 nanosheets, the center temperature of the furnace was 450°C. Nitrogen was used as the carrier gas with a flow rate of ~100 sccm. (b) Optical image of an as-

synthesized 2D Bi_2S_3 nanosheets on SiO_2/Si substrate. (c, d & e) The crystal structure of Bi_2S_3 viewed from three axes (f) AFM image of a typical as-grown 2D Bi_2S_3 nanosheet on a SiO_2/Si substrate, and (g) height profile recorded along the red line in (f).

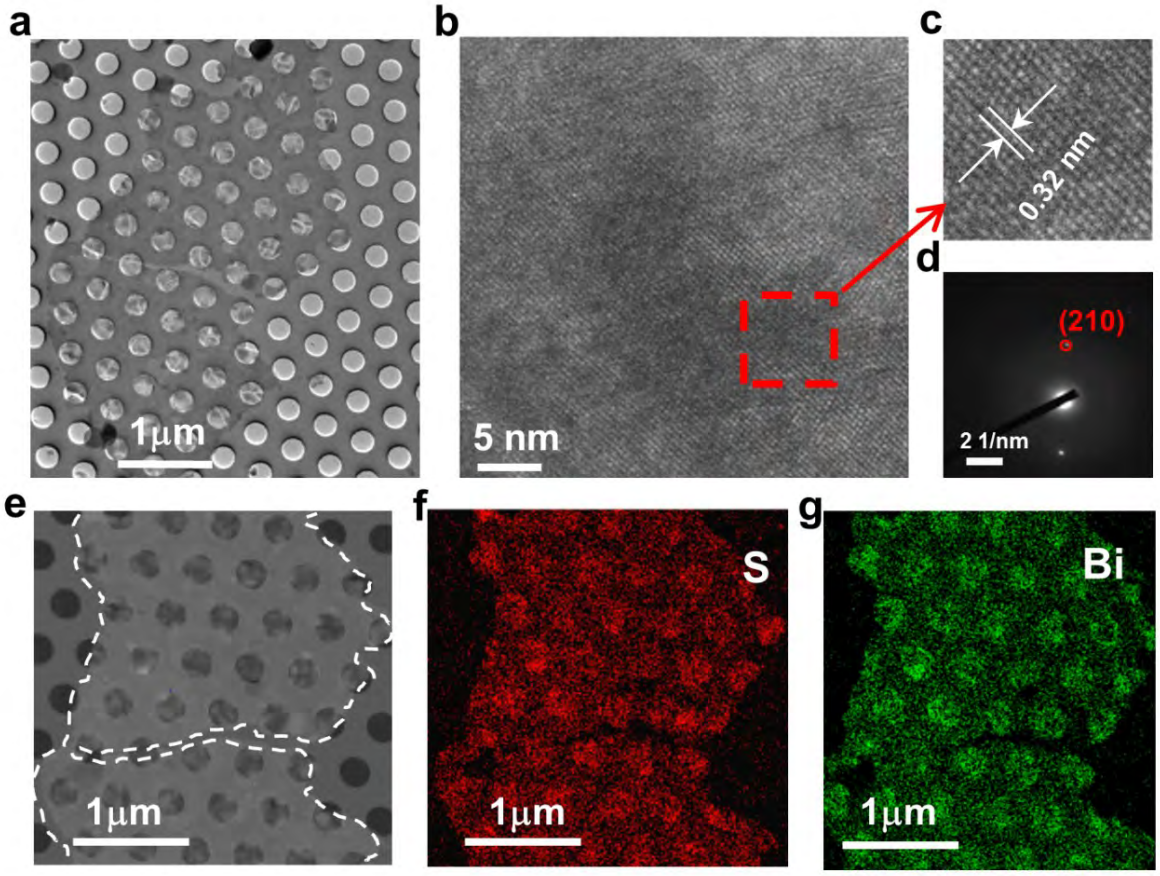

Figure 2. (a) TEM image of a Bi_2S_3 nanosheet. (b) HRTEM image (c) Magnified HRTEM image illustrating the observed crystal spacing. (d) SAED pattern of a synthesized nanosheet (e) Low magnification dark-field TEM image (f and g) Elemental composition maps for sulfur (red) and bismuth (green).

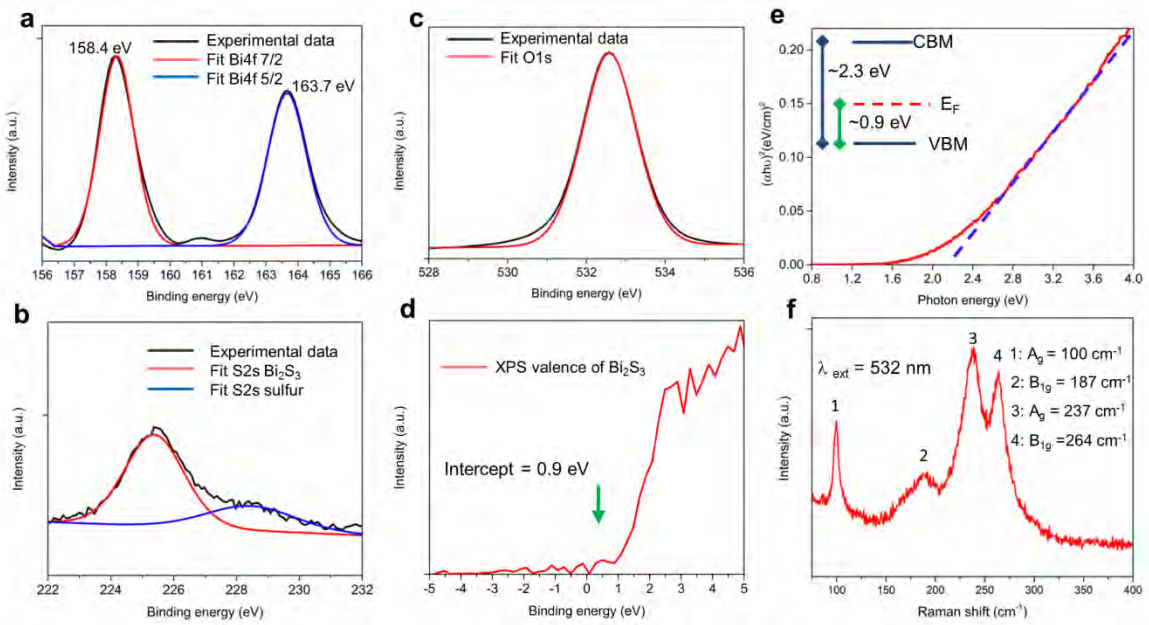

Figure 3. (a) XPS spectrum of Bi_2S_3 nanosheets where the peaks at ~158.4 eV and ~163.7 eV are associated with the Bi 4f $_{7/2}$ and Bi 4f $_{5/2}$ electrons, respectively. (b) The peak located at 225.1eV corresponds to the S 2s electrons in Bi_2S_3. (c) XPS oxygen spectrum featuring only the O 1s peak associated with the SiO_2 substrate, while no Bi_2O_3 peak at ~530 eV is evident. (d) XPS valence band spectrum shows an intercept at 0.9 eV, suggesting that the material is slightly p-type. (e) UV-Vis Tauc plot revealing a direct optical bandgap of 2.3 eV. (f) Raman spectrum of the 2D nanosheet with the four Bi_2S_3 modes (transverse and longitudinal A_g and B_{1g} modes) being highlighted.

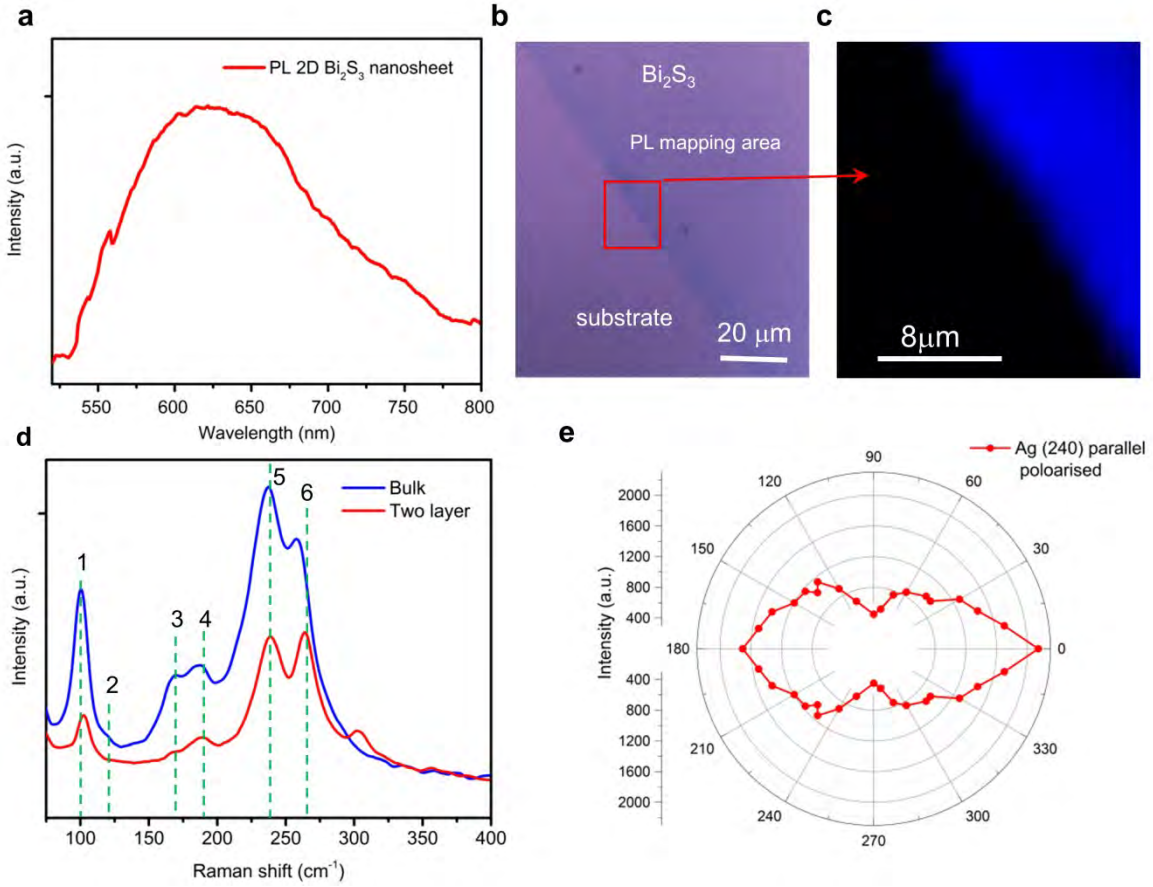

Figure 4. (a) PL spectrum of a bilayer Bi_2S_3 nanosheet. (b) Optical image of a 2D nanosheet. (c) PL intensity map of the 2D nanosheet depicted in the optical image. (d) The Raman spectrum of bulk Bi_2S_3 (blue line) and the synthesized 2D nanosheets (red line). (e) Intensity contour map of the A_g mode as a function of excitation laser polarization angle.

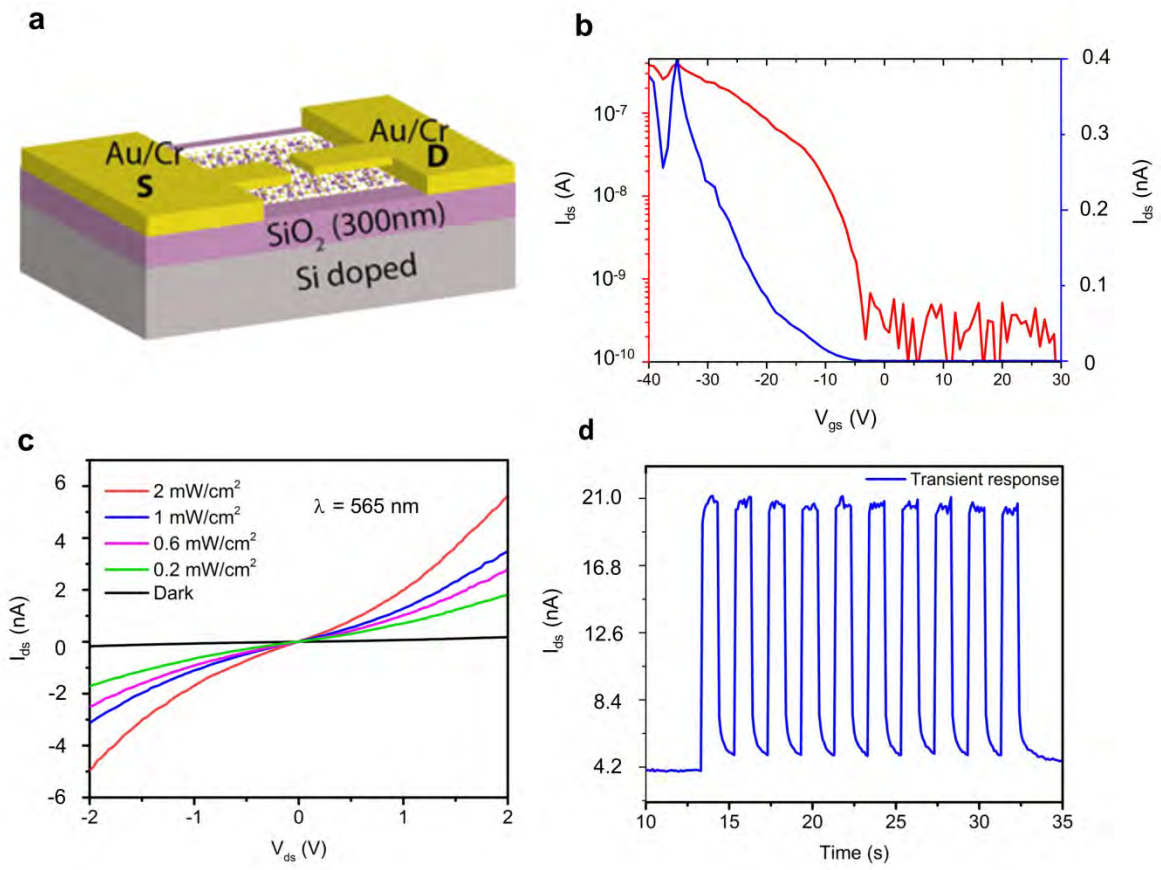

Figure 5. Bi_2S_3 nanosheet FET device performance. (a). schematic of the FET device. (b) Transfer characteristic I_{ds}-V_{bg} in log and linear scale of Bi_2S_3 FET. (c) I-V curves of photodetector illuminated with different power density of light (wavelength 565 nm). (d) Transient response of photodetector where V_{ds} = 1V, wavelength of light 565 nm at 2 mW/cm^2, pulsed at 1Hz.

TOC

This work broadens the scalable synthesis and application of anisotropic 2D Bi_2S_3 nanosheets for potential optoelectronic devices. The synthesis method results in large lateral size nanosheets of Bi_2S_3 which are highly in-plane anisotropy and p-type semiconductivity. Photodetection and field effect transistor devices with 2D Bi_2S_3 channel exhibit a good responsivity of 8 AW^{-1} and a maximum mobility of 28 $cm^2V^{-1}s^{-1}$.